



**HAL**  
open science

# Highly Nonlinear Multimode Tellurite Fibers: From Glass Synthesis to Practical Applications in Multiphoton Imaging

Marianne Evrard, Tigran Mansuryan, Vincent Couderc, Frédéric Désévéday, Clément Strutynski, Marc Dussauze, Yago Arosa Lobato, Alessandro Tonello, Maggy Colas, Georges El-Dib, et al.

► **To cite this version:**

Marianne Evrard, Tigran Mansuryan, Vincent Couderc, Frédéric Désévéday, Clément Strutynski, et al.. Highly Nonlinear Multimode Tellurite Fibers: From Glass Synthesis to Practical Applications in Multiphoton Imaging. *Advanced Photonics Research*, 2023, 4 (1), pp.2200213. 10.1002/adpr.202200213 . hal-04151622

**HAL Id: hal-04151622**

**<https://hal.science/hal-04151622>**

Submitted on 20 Aug 2024

**HAL** is a multi-disciplinary open access archive for the deposit and dissemination of scientific research documents, whether they are published or not. The documents may come from teaching and research institutions in France or abroad, or from public or private research centers.

L'archive ouverte pluridisciplinaire **HAL**, est destinée au dépôt et à la diffusion de documents scientifiques de niveau recherche, publiés ou non, émanant des établissements d'enseignement et de recherche français ou étrangers, des laboratoires publics ou privés.



Distributed under a Creative Commons Attribution 4.0 International License

# Highly Nonlinear Multimode Tellurite Fibers: From Glass Synthesis to Practical Applications in Multiphoton Imaging

Marianne Evrard,\* Tigran Mansuryan, Vincent Couderc, Frédéric Désévéday, Clément Strutynski, Marc Dussauze, Yago Arosa Lobato, Alessandro Tonello, Maggy Colas, Georges El-Dib, Sylvain Danto, Thierry Cardinal, and Frédéric Smektala

Herein, a tellurite multimode optical fiber with a rectangular step-index core to combine easy coupling of the pump power with the exceptionally cubic nonlinearity of such type of glass is developed. An alkali-free composition ( $\text{TeO}_2\text{-ZnO-L}_2\text{O}_3$ ) is prepared to produce a preform with the use of both the stack-and-draw and the direct-bonding methods. The linear and nonlinear optical responses of the fiber are characterized and are then used to generate a homogeneous supercontinuum (SC) in the near-infrared domain. The spectral broadening, which is obtained in this work in a short fiber sample, is used for imaging mouse kidney cells, labeled with three different fluorochromes, by means of two-photon absorption (2PA) and three-photon absorption (3PA). Despite the multimode nature of the output beam, clear images of tubules, actin, and nucleus are collected with a spatial resolution down to  $1.2\ \mu\text{m}$ . Although image acquisition at better resolution has already been reported in the literature using relatively long spans of graded-index silica multimode fibers, here, the combination of high third-order susceptibility of the glass and the large Raman gain in short segments of tellurite fiber is exploited to obtain nonlinear imaging with adequate spatial resolution.

supercontinuum (SC) spectra.<sup>[2]</sup> In particular, SC generation with wavelengths covering all the visible domain and a large part of the silica transparency window has been demonstrated<sup>[3]</sup>: the spatially single-mode polychromatic beams have widely been employed for linear and nonlinear fluorescence imaging using femtosecond, picosecond, or subnanosecond pulses.<sup>[4,5]</sup> More recently, multimode optical fibers have also been considered for efficient imaging processes demonstration in the visible and near-infrared domain<sup>[6]</sup>; in particular, two and three-photon fluorescence measurements have been demonstrated. Although coupling laser light into a multimode fiber is a relatively easy task, the output beam suffers from spatial and temporal distortions that bring severe limitations to the imaging resolution. Such drawback may be mitigated using optimization techniques such as deep-learning algorithms combined with spatial light modulators<sup>[7]</sup>;


## 1. Introduction

Multimodal imaging, which can be defined as the simultaneous production of multiple signals from different imaging techniques, has been significantly boosted in the past 20 years thanks to the advent of microstructured optical fibers<sup>[1]</sup> which allows the conversion of narrowband powerful infrared lasers, into

one can also take advantage of nonlinear effects such as the spatial beam self-cleaning, already reported in the literature also for non-silica graded-index multimode fiber,<sup>[8]</sup> to reach nearly single-mode output beam, and consequently high transverse resolution images. However, the large core diameter of the multimode fiber requires the use of long spans to obtain significant spectral broadening, owing to the relatively low nonlinear

M. Evrard, F. Désévéday, C. Strutynski, F. Smektala  
Laboratoire Interdisciplinaire Carnot de Bourgogne  
UMR 6303 CNRS-Université de Bourgogne-Franche-Comté  
9 Avenue Alain Savary, 21078 Dijon, France  
E-mail: marianne\_evrard@etu.u-bourgogne.fr

T. Mansuryan, V. Couderc, Y. Arosa Lobato, A. Tonello  
Institut de Recherche XLIM  
UMR 7252 CNRS-Université de Limoges  
123 Avenue Albert Thomas, 87060 Limoges, France

 The ORCID identification number(s) for the author(s) of this article can be found under <https://doi.org/10.1002/adpr.202200213>.

© 2022 The Authors. Advanced Photonics Research published by Wiley-VCH GmbH. This is an open access article under the terms of the Creative Commons Attribution License, which permits use, distribution and reproduction in any medium, provided the original work is properly cited.

DOI: 10.1002/adpr.202200213

Y. Arosa Lobato  
Departamento de Física Aplicada  
University of Santiago de Compostela  
Praza do Obradoiro S/N, 15782 Santiago de Compostela, A Coruña, Spain

M. Dussauze  
Institut des Sciences Moléculaires  
UMR 5255 CNRS-Université de Bordeaux  
351 Cours de la Libération, 33405 Talence, France

M. Colas  
UMR 7315 CNRS-Université de Limoges  
Centre Européen de la Céramique  
Institut de Recherche sur les Céramiques  
12 Rue Atlantis, 87068 Limoges, France

G. El-Dib, S. Danto, T. Cardinal  
Institut de Chimie de la Matière Condensée de Bordeaux  
UMR 5036 CNRS-Université de Bordeaux  
87 Avenue du Dr Albert Schweitzer, 33608 Pessac, France

coefficient of silica glass. Consequently, modal and chromatic dispersion tend to spread the optical pulses reducing their peak intensities: one way to thwart such limitation is to use multimode fibers based on highly nonlinear glasses, to reach significant spectral broadening in only a few tens of centimeters of propagation, reducing the impact of dispersion.

In this perspective, heavy metal-oxide glasses, including tellurite glasses, show interesting optical properties, for instance, high nonlinear indices (around  $4.10^{-19} \text{ m}^2 \text{ W}^{-1}$ , which appears to be 18 times higher than for silica), and mid-infrared transparency (from visible to  $\approx 6.5 \mu\text{m}$ ). These properties<sup>[9,10]</sup> allow tellurite fibers to represent an attractive alternative for SC generation<sup>[11]</sup> and mid-infrared laser sources.

In a previous work, the  $\text{TeO}_2\text{-ZnO-La}_2\text{O}_3$  (TZL) ternary diagram was investigated<sup>[12]</sup> by the authors to identify core and cladding alkali-free compositions for step-index fiber manufacturing. Based on optical and thermomechanical properties, core and cladding glass compositions have been selected and step-index fibers have been drawn. However, a limited transmission range was reported for these fibers so far, related to the OH contamination occurring at  $3.3 \mu\text{m}$ . Recently, a purification process has been applied to these glasses, significantly improving their transmission.<sup>[13]</sup>

Moreover, it has been recently demonstrated how rectangular core fibers can offer interesting features such as high birefringence or superior thermal management with respect to conventional fibers, since the heat removal is facilitated by the long dimension of the core, which in turn increases the maximum power throughput. This fact opens new perspectives for laser amplification by mode conversion.<sup>[14,15]</sup>

In the present study, multimode rectangular-section tellurite fibers have been manufactured for specific nonlinear optics experiments, such as SC generation. It is important to note that this work mainly focuses on the exploitation of the nonlinear properties from the multimode rectangular-section tellurite fibers although the multimode profile and the rectangular core shape are not here necessary conditions for the experiments. The elaboration of fibers by the modified stack-and-draw technique also provides a powerful alternative to the usual fiber production methods since there is no more need to drill the glass, which weakens the structure of the preform and complicates the drawing due to the presence of possible fissures. The preform is prepared by the stack-and-draw method and is then thermally drawn, reducing homotetically the core dimensions. Once the fiber is ready, the linear losses and the nonlinear response of such multimode rectangular-core fiber are characterized. The large core area of such fiber simplifies the coupling with infrared laser with no need for precise 3D mechanical mounts. The all-normal dispersion regime in the near-infrared domain and the

Raman gain profile can also favor, in femtosecond and picosecond regimes, the generation of a homogeneous and asymmetrical spectral broadening, particularly suitable for two- and three-photon nonlinear fluorescence imaging.

## 2. Preparation and Characterization of Rectangular-Core Tellurite Fibers

### 2.1. Glass Formulation

Core and cladding compositions are selected from the previously studied TZL vitreous ternary diagram.<sup>[12]</sup> The core glass composition is  $70\text{TeO}_2\text{-}25\text{ZnO}\text{-}5\text{La}_2\text{O}_3$  (TZL 70-25-05), while the cladding glass is  $65\text{TeO}_2\text{-}30\text{ZnO}\text{-}5\text{La}_2\text{O}_3$  (TZL 65-30-05). The main thermal properties of the core and cladding glasses are summarized in **Table 1**. It is worth mentioning that the considered materials are synthesized using the melt-quenching technique (see the experimental section for more details). The core and cladding compositions are chosen so that they possess similar thermal properties (comparable characteristic temperatures and thermal expansion coefficients) and share a wide common drawing temperature range, which makes them suitable for co-drawing. We take advantage of the material compatibility criterion for the development of unprecedented tellurite fiber profiles as it is described in the next Section 2.2.

### 2.2. Preform Preparation and Drawing

Previous works have shown that the well-known stack-and-draw method can be applied not only for the production of cylindrical fiber geometries, but also for the development of unusual all-glass or multi-material elongated architectures.<sup>[16]</sup> In this section, we take advantage of the stack-and-draw method to prepare a rectangular-section preform. Five vitreous tellurite glass plates (one core cane and four cladding plates) are processed and assembled to build the preform as described in **Figure 1a–I**. Two kinds of vitreous cladding plates are used here: top and bottom plates have  $10 \times 3 \times 40 \text{ mm}$  dimensions (width, thickness, and length), while the lateral plates measure  $3 \times 6 \times 40 \text{ mm}$ . The core cane dimensions are  $4 \times 6 \times 40 \text{ mm}$ . All those parts are carefully polished to improve the surface quality and optimize the surface contacts within the stack. A thermal consolidation is then performed on the assembly before the fiber drawing. It consists in heating the stack for 6 h at  $T_{\text{g}}(\text{cladding}) + 45 \text{ }^\circ\text{C}$  (i.e.  $420 \text{ }^\circ\text{C}$ ) while applying a moderate strain ( $\approx 1.2 \text{ kPa}$ ) on it, by means of a piece of brass of a few tens of grams which has been placed on the preform, previously wrapped within a platinum sheet to avoid any contamination of the glass parts

**Table 1.** Transition temperature ( $T_{\text{g}}$ ), onset temperature for the first crystallization exothermic peak ( $T_{\text{x}}$ ), thermal stability ( $\Delta T$ ), thermal expansion coefficient (TEC) and drawing temperature range ( $T_{\text{Draw}}$ ) for the fiber core and cladding compositions.

Composition [mol%]	$T_{\text{g}}$ ( $\pm 2 \text{ }^\circ\text{C}$ )	$T_{\text{x}}$ ( $\pm 2 \text{ }^\circ\text{C}$ )	$\Delta T$ ( $\pm 4 \text{ }^\circ\text{C}$ )	TEC [ $^\circ\text{C}^{-1}$ ]	$T_{\text{Draw}}$ [ $^\circ\text{C}$ ]
TZL 70-25-05 (core)	365	525	160	$19.4 \times 10^{-6}$	430–480
TZL 65-30-05 (clad)	375	–	>100	$20.2 \times 10^{-6}$	440–490

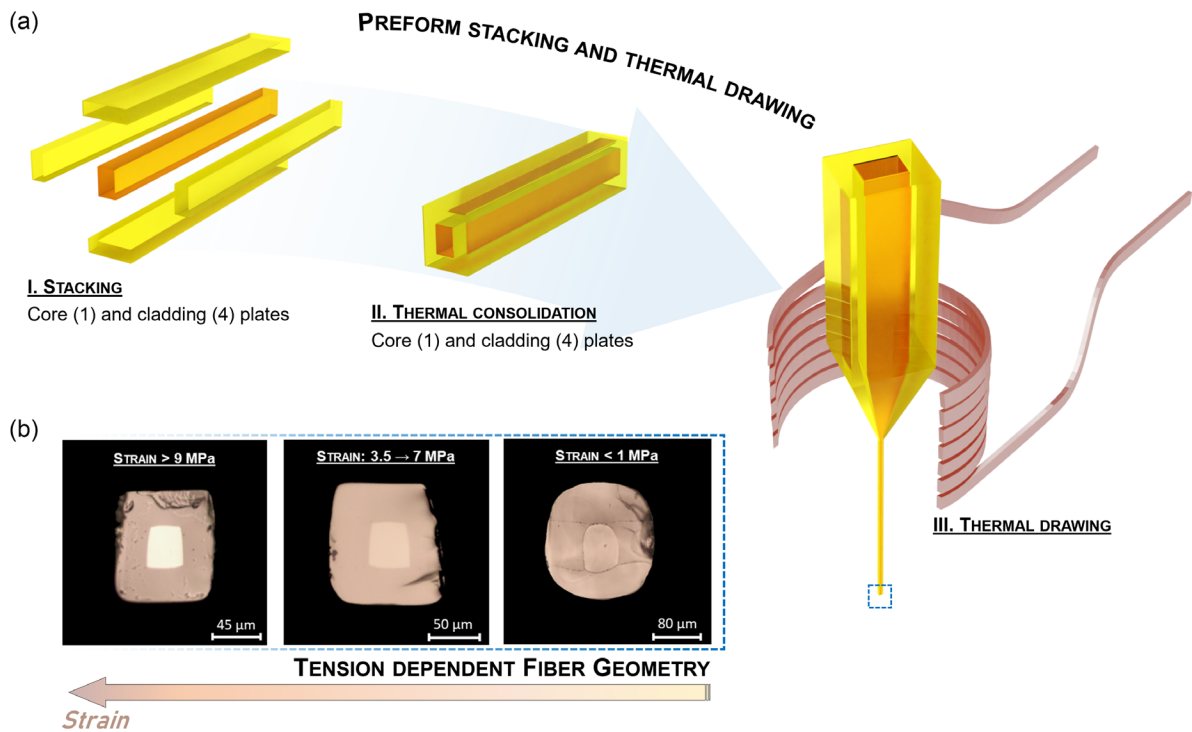


**Figure 1.** a) Description of the rectangular-section fiber manufacturing process and b) evolution of the fiber section geometry as a function of the applied strain during thermal drawing. (Micrographs were captured by using an optical microscope in transmission mode.)

from the brass and ceramic elements (supports) used during the treatment. This consolidation procedure derives from the “Direct-Bonding Method”,<sup>[17]</sup> which refers to the adhesion of two solid materials with flat, smooth, and clean surfaces, by van der Waals or hydrogen-like bonds. It has mostly been exploited for silicon–silicon or silica–silicon wafers bonding, but several works demonstrated that tellurite glass films can be bonded to silicate substrates using the same methodology: hydrogen bonds (with high relative humidity) or Te–O bonds (with O from silica, for lower relative humidity) are reported. In the present case, the consolidation is expected to improve adhesion between the glass parts by promoting the formation of Te–O–Te bonds at their interfaces, which results from the reaction of surface Te–OH groups (comparably to Si–OH recombinations into Si–O–Si).<sup>[18]</sup> More importantly, this procedure provides the required level of cohesion to the final preform to be thermally stretched without suffering any deformation or detachment of the different parts. The main steps of the manufacturing process of the rectangular-section preform and its drawing are illustrated in Figure 1a. Pictures of the fiber obtained for different ranges of drawing stress are presented in Figure 1b. The drawing stress is directly related to the temperature at which the thermal stretching of the preform is performed, because it greatly influences the glass flowing ability due to the temperature dependence of viscosity. In the present case, it is noticeable that precise control of the drawing stress, and therefore temperature, is necessary to maintain the desired rectangular fiber geometry. Indeed, the starting preform profile is completely deformed when the fiber fabrication is done at a

drawing stress lower than  $\approx 1$  MPa. In that case, the structure drifts towards a cylindrical shape, most likely due to surface tension effects that occur during the flowing of the glass. For drawing stresses between 3.5 and 7 MPa, the rectangular structure is well preserved, but with minor deformations (round edges and moderately deformed core-cladding interfaces). Finally, the geometry slightly improves for drawing stress higher than  $\approx 9$  MPa. The fiber drawing being a homothetic process, the preform geometry and height-to-width ratio are also expected to be preserved and directly transferred to the fiber. In the present work, the preform section has a 1.20 height–width ratio ( $10 \times 12$  mm section) while it is  $\approx 1.18$  ( $85 \times 100$   $\mu\text{m}$  section) on the fiber. In the end, with adequate control of the glass viscosity, it is demonstrated here that sharp corner-edges rectangular core fibers can be produced from the stack-and-draw method.

The fiber optical losses have been measured at 1030 nm (with a laser Diadem from Spark Lasers) in a few tens of centimeters long rectangular fiber: the attenuation is found to be  $\approx 15$  dB  $\text{m}^{-1}$ . This value is typical of tellurite fibers prepared under room atmosphere conditions and in absence of particular care.<sup>[19,20]</sup> Moreover, the imperfections at the interfaces between the core and cladding cause higher optical losses. They are mainly voids due to the stack-and-draw manufacturing process, i.e., because of non-optimized contacts between the different pieces that are used to build the preform. Indeed, these cavities are not completely eliminated during the thermal drawing process and are transferred to the fiber which increases the optical attenuation of the signal. These losses can be lowered by optimizing the preform preparation process to improve the

core/cladding interfaces (better cutting and polishing procedures, applying a vacuum during the consolidation or the thermal elongation process, etc.). The use of high-purity precursors and performing the glass synthesis under a dry and monitored atmosphere will also contribute to optical loss reduction. The latter will also allow to expand the transmission range up to 3  $\mu\text{m}$  by reducing OH concentration in glass and fiber.<sup>[13]</sup> In the following sections, rectangular fibers with a  $90 \times 110 \mu\text{m}$  outer dimensions and a  $30 \times 35 \mu\text{m}$  core are considered.

### 2.3. Characterizations of the Raman Gain and SC Generation

In this section, the Raman gain coefficients of both core and cladding glassy compositions have been determined from spontaneous Raman scattering spectra measured at two wavelengths: 532 and 785 nm. Such characterization is of great interest to evaluate the nonlinear optical response of these glasses and as a consequence for the SC study, notably for the spectral broadening numerical simulation which will be presented in the following. The complete methodology for the Raman gain quantification is described in the Experimental Section. Raman gain coefficients

calculated relative to  $\text{SiO}_2$  are summarized in Table 2, while profiles are plotted in Figure 2. The Raman gain spectra of core and cladding compositions, respectively, for the 532 nm- (Figure 2a) and the 785 nm excitation (Figure 2b) are plotted as a function of the conventional Raman shift. Figure 2c is specific for the core composition, while Figure 2d is the equivalent for the cladding composition, with the Raman gain spectra obtained for both the 532 nm excitation and the 785 nm excitation. The x-axis is here scaled with absolute values of wavelengths.

Raman gain coefficients for both TZL compositions are 45 times higher than fused-silica at 532 nm, and 24 times higher at 785 nm (taking as reference values  $g_{\text{R}(\text{SiO}_2)} = 1.86 \times 10^{-13} \text{ m W}^{-1}$  and  $g_{\text{R}(\text{SiO}_2)} = 1.2 \times 10^{-13} \text{ m W}^{-1}$  at 532 and 785 nm, respectively<sup>[21,22]</sup>). Such Raman scattering cross-section dependence versus wavelength is expected: the dispersion of the Raman gain which is illustrated in Figure 2c,d is a well-known phenomenon.<sup>[23–25]</sup>

For the tellurite glassy compositions developed in this study, the dispersion of Raman gain coefficients corresponds well with the dispersions reported for the glasses  $85\% \text{TeO}_2$ – $10\% \text{Nb}_2\text{O}_5$ – $5\% \text{MgO}$  and  $85\% \text{TeO}_2$ – $15\% \text{WO}_3$  in a range of excitation wavelength varying from 450 to 1064 nm.<sup>[26]</sup>

**Table 2.** Refractive indices and Raman gain coefficient, normalized to  $\text{SiO}_2$ , with excitation wavelengths at 532 and 785 nm.

Composition [mol%]	Refractive index $n(\lambda)$ ( $\pm 1 \times 10^{-3}$ )				Raman Gain coefficient [ $\text{m W}^{-1}$ ] (Mode position: $\approx 760 \text{ cm}^{-1}$ )	
	543.5 [nm]	632.8 [nm]	1064 [nm]	1550 [nm]	532 [nm] (excitation)	785 [nm] (excitation)
TZL 70-25-05 (core)	2.068	2.042	2.005	1.999	$83 \times 10^{-13}$ ( $\pm 10\%$ )	$28 \times 10^{-13}$ ( $\pm 10\%$ )
TZL 65-30-05 (clad)	2.047	2.022	1.986	1.980	$84 \times 10^{-13}$ ( $\pm 10\%$ )	$29 \times 10^{-13}$ ( $\pm 10\%$ )

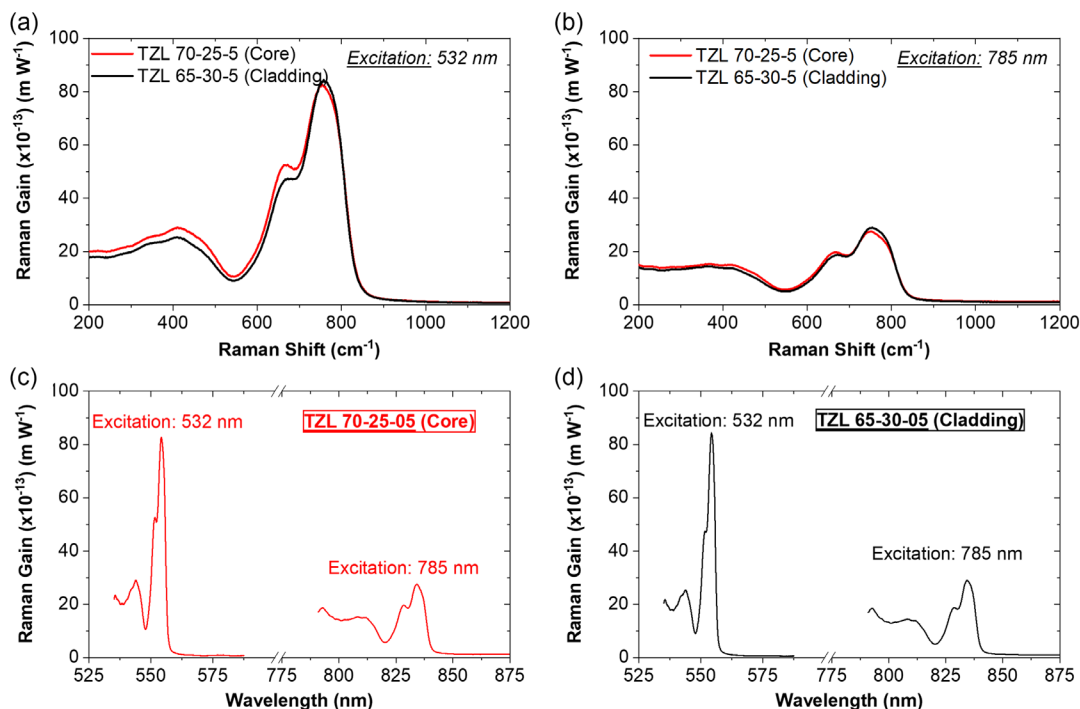


**Figure 2.** Raman gain spectra, normalized to  $\text{SiO}_2$ , with pump wavelengths at: a) 532 nm and b) 785 nm for: c) core and d) cladding compositions.

In absolute values, although little data are reported in the literature for tellurite glasses for the exact same excitation wavelengths some values can be employed for comparison: the Raman gain coefficients of TZL glasses are very close to the one of  $\text{Nb}_2\text{O}_5\text{-TeO}_2$ <sup>[26]</sup> and  $\text{Ta}_2\text{O}_5\text{-TeO}_2$ <sup>[27]</sup> glassy systems, around 25% lower than the  $\text{WO}_3\text{-TeO}_2$  system<sup>[26]</sup> and 50% lower than for  $\text{TeO}_2\text{-TiO}_{0.5}$  glassy compositions.<sup>[28]</sup> Thus, the strength of the Raman gain observed here is not as strong as for tellurite glasses formed with heavy metals having incomplete s-electron pairs, such as thallium, or incomplete d-shell metals such as niobium, tungsten, or tantalum oxide but it presents higher values than tellurite glasses modified by the use of less polarizable compounds, such as  $\text{Na}_2\text{O}$  or  $\text{ZnO}$ .<sup>[29]</sup> In addition, one should point out that for the present TZL glasses a significantly low Te atoms density ( $\approx 1.5 \cdot 10^{22}$  Te atoms  $\text{cm}^{-3}$ ) as compared to all the tellurite glassy compositions which have been reported for their Raman gain coefficients.<sup>[26,27,29]</sup> It denotes that the addition of lanthanum oxide in a tellurite glassy system allows keeping strong Raman gain values but also provides good fiber drawing capacities constituting a combination of properties of interest.

SC generation is then studied from a 33 cm-long tellurite rectangular-core fiber (Figure 3) with  $30 \times 35 \mu\text{m}$  transverse dimensions by using a Spark Diadem laser with a 1030 nm wavelength. The pulse duration was varied from 300 fs to 3 ps with a repetition rate of 30 kHz. The available average power is 55 mW, which represents more than 6.1 MW of peak power for 300 fs pulse duration. The initial pump beam diameter is close to  $20 \mu\text{m}$  (full width at half maximum in intensity–FWHMI). Because of the normal dispersion regime at 1030 nm, the spectral broadening of the multimodal beam is mainly governed by self-phase modulation combined with Raman gain, which leads

to an asymmetric spectrum (see Figure 3). The large Raman gain of the glass, which is 45 times higher than that of silica as well as its spectral shape covering more than  $800 \text{ cm}^{-1}$  facilitates the spectral broadening toward the infrared domain.

We obtained a SC spanning from 700, up to 1650 nm at the maximum pump peak power of 6.1 MW. However, it can be underlined that the output spectrum evolves slowly between 2.2 and 6.1 MW. Thus, for the maximum peak power, the glass begins to progressively damage without observing any plasma generation which is different from what happens in silica multimode fibers.<sup>[30]</sup> The output spatial beam shape creates a speckled pattern, which is marginally influenced by the variation of the input pump peak power (see the insets of Figure 3). The input average and peak powers of our laser source can be modified by adjusting both repetition rate (from 0 to 2 MHz) and pulse duration (from 300 fs to 100 ps). The envelope of the infrared SC remains unchanged for a pulse duration between 300 fs and 3 ps, when we maintain a constant peak power.

The initial steps of the spectral broadening in the TZL rectangular waveguide have also been numerically studied by using a generalized nonlinear Schrödinger equation that takes into account the beam diffraction, the wavelength dependence of the refractive index, the waveguide contribution, the instantaneous and delayed Raman nonlinear response of the TZL glass thanks to the Raman gain measurements previously determined and reported in this article. From a nonlinear perspective, the square fiber with a step refractive index core profile should present a natural self-imaging process solution that can periodically modulate the pump beam facilitating the occurrence of geometric parametric instabilities<sup>[31]</sup> and therefore nonlinear conversions over a large spectral domain. However, no irrefutable

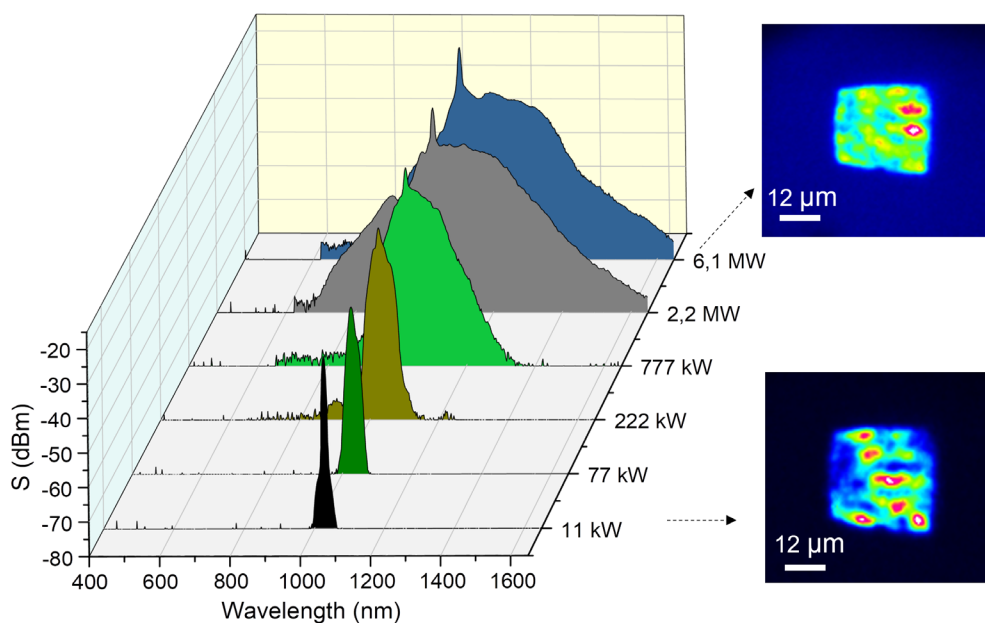


**Figure 3.** Experimental results of supercontinuum (SC) generation versus input peak power. Repetition rate: 30 kHz; Insets: output beam shape for 6.1 MW (top) and 11 kW (bottom).

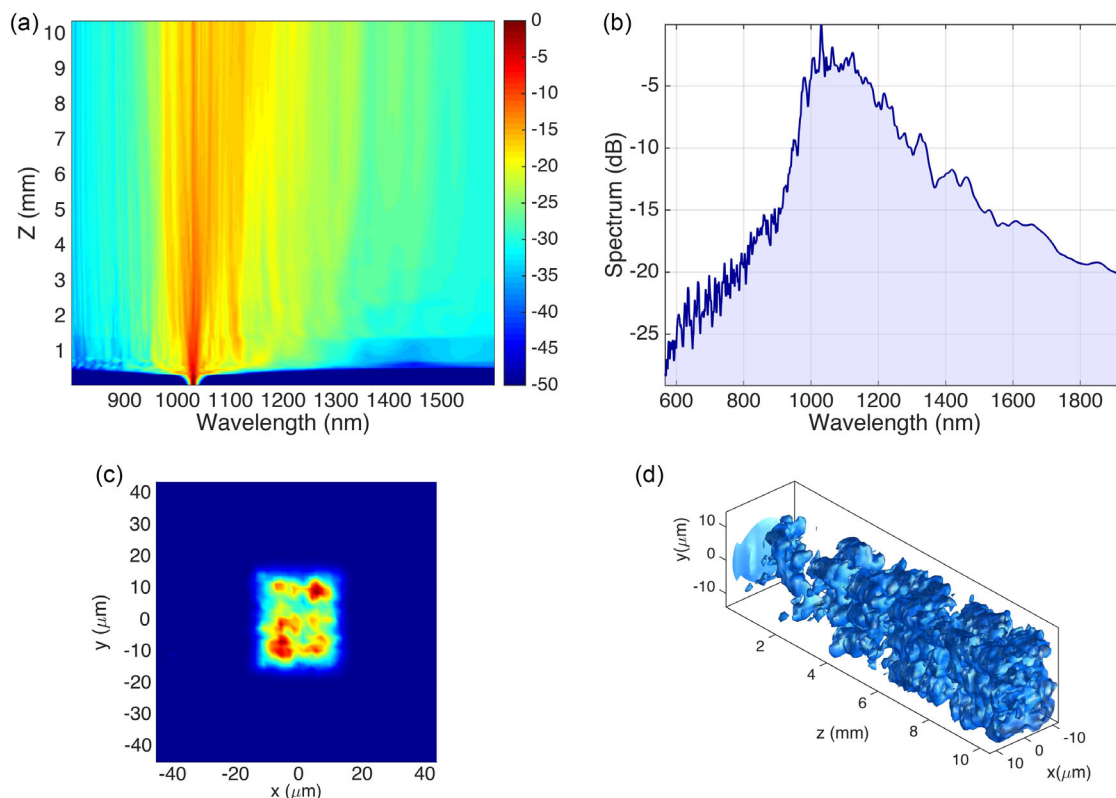


**Figure 4.** Numerical simulations of spectral broadening in rectangular core tellurite fiber. a) Spectral evolution of the nonlinear broadening versus the propagation length for an input peak power of 0.5 MW; b) example of output spectral shape after 1 cm of propagation ( $I_{IN} = 136 \text{ GW cm}^{-2}$ ); c) example of the spatial output beam profile ( $z = 10 \text{ mm}$ ); d) evolution of the spatial energy distribution in the first millimeters of propagation.

evidence of that process is clearly observed in the experimental results. Thus, the experiment description is simplified without claiming the implication of that process in the SC. **Figure 4** summarizes the numerical results for an input beam with a diameter of  $18 \mu\text{m}$  FWHMI, pulse duration of 300 fs, and input peak intensity of  $136 \text{ GW cm}^{-2}$ .

In qualitative agreement with the experimental results, the initial steps of the numerical simulations predict symmetrical spectral broadening, owing to the self-phase modulation (causing also spatial beam focusing), which is the dominant nonlinear effect. After 1 cm of propagation, in the multimode optical fiber, the temporal pulse envelope is of 920 fs (FWHMI).

Similar to the experimental results, which showed how beyond 200 kW of peak power the Raman gain comes into play, the numerical spectrum shape grows asymmetrically toward the longer wavelengths covering, in the end, more than 800 nm in the near-infrared domain. In spite of the large core area, the beam intensity is large enough to generate a rather homogeneous spectrum, with a speckled output beam pattern.

It is also important to note that because of the high nonlinear index of the TZL glass ( $4 \times 10^{-19} \text{ m}^2 \text{ W}^{-1}$  which is more than 18 times higher than the silica glass), the spectral broadening is mainly obtained in the first centimeters of the propagation (see **Figure 4a**). The output beam profile is clearly multimode with an  $M^2$  close to 2.

### 3. Multimodal Imaging

#### 3.1. Experimental Setup for Nonlinear Fluorescence Imaging

After SC generation, the output polychromatic beam is collimated by means of a convergent lens ( $f = 15 \text{ mm}$ ). A neutral density filter is placed at the input of the microscope to control the power sent to samples. A long-pass filter FELH1100 (Thorlabs) is first used to select the desired wavelength bands between 1100 and 1700 nm. The filtered beam is sent in an upright multiphoton microscope (Bergamo-Thorlabs) equipped with galvanometric scanners and two photo multipliers (**Figure 5**). The incident beam is focused on the sample with an Olympus XLUMPLFLN20XW objective. Bandpass filters are placed in front of the photomultiplier tubes, to select the fluorescence emission. Images with  $1024 \times 1024$  pixels are obtained with a dwell time of  $5 \mu\text{s px}^{-1}$  with twenty accumulations.

#### 3.2. Mouse Kidney Cells Characterization

Mouse kidney cells are observed using multiphoton imaging, following the previously described setup. A slide *Invitrogen FluoCells n°3 F24630* with three fluorochromes labeling cells is employed. Tubules are labeled with Alexa 488, actin with Alexa 568, and nucleus with DAPI. For wavelengths excitation between 1070

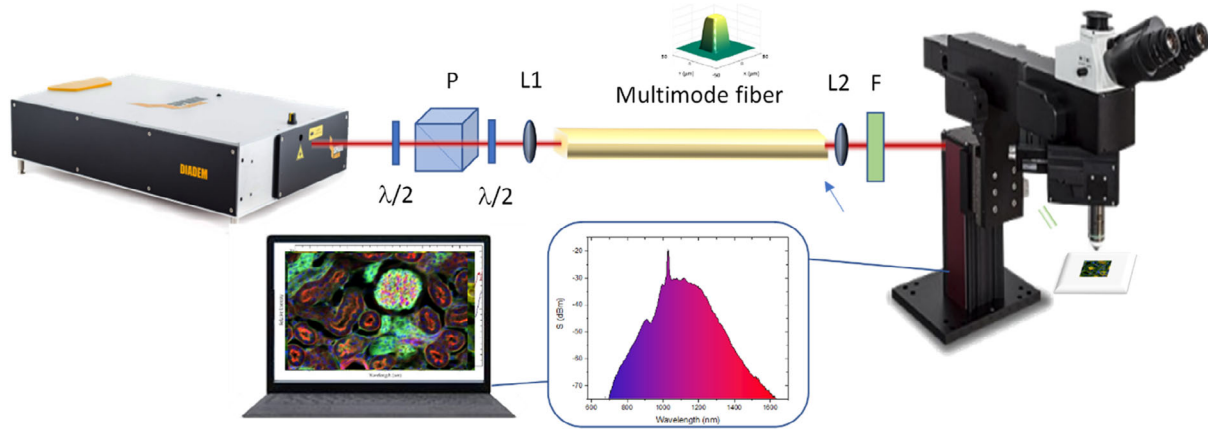


**Figure 5.** Experimental setup used for an imaging application.

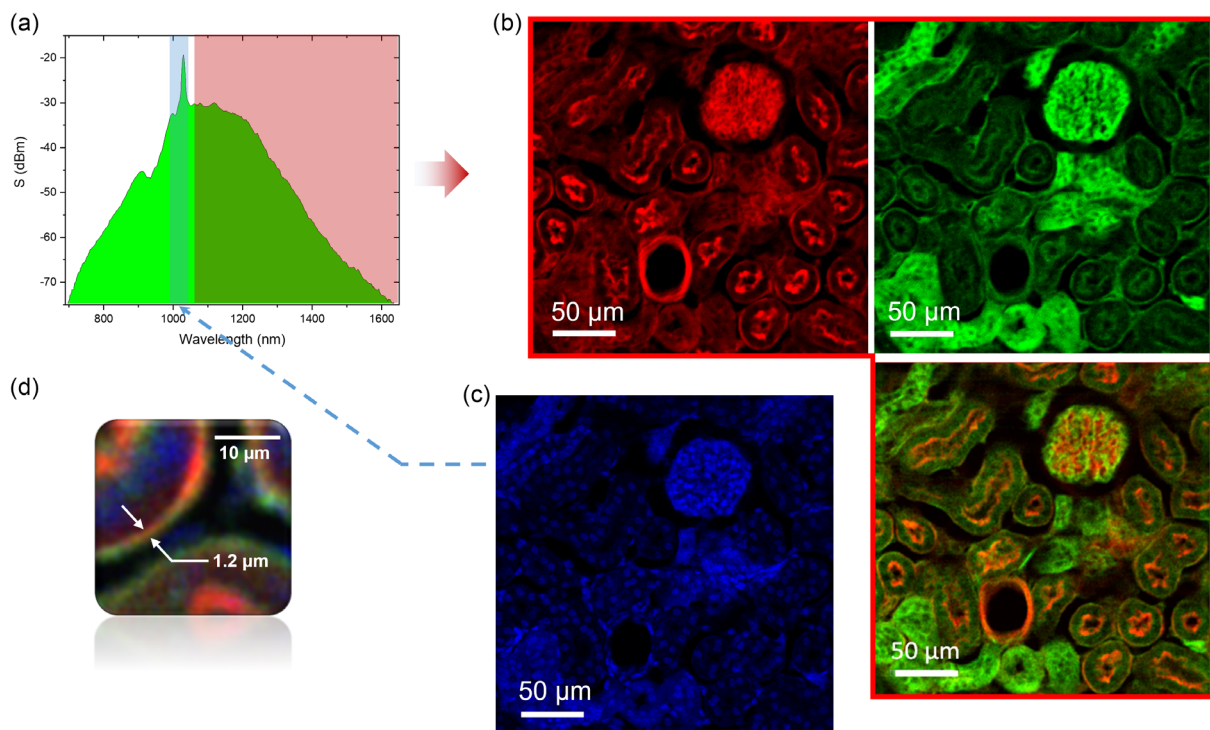


**Figure 6.** a) Broadband spectrum with the two filtered parts used for nonlinear fluorescence imaging. b) Two-photon absorption (2PA) images of actin (red), tubules (green), and superimposition of both images (bicolor image). c) Three-photon absorption (3PA) images of the nucleus excited with the residual pump beam at 1030 nm. d) Resolution of our system, evaluated with the observation of the smallest element clearly visible on a multicolor image.

and 1700 nm, we obtained images of tubules and actin with a two-photon absorption (2PA) configuration (see **Figure 6b**). The image of the nucleus has been only collected by adding the residual pump beam at 1030 nm which corresponds to the three-photon absorption (3PA) experiment (**Figure 6c**). Filters Semrock 469/35, Semrock 509/22, and Semrock 607/70 are used to select the fluorescence coming from DAPI, Alexa 488, and Alexa 568, respectively. In such configuration and using this multimode optical fiber details as small as 1.2 μm have been observed by lighting the sample with an infrared beam (1100–1700 nm): this corresponds, on average, to a resolution

close to the wavelength dimension (**Figure 6d**), which is only twice times larger than the half-wavelength minimum resolution reported with a single-mode polychromatic beam.<sup>[6]</sup>

#### 4. Conclusion

We demonstrated that the stack-and-draw technique combined with the direct-bonding method enables the rather straightforward fabrication of rectangular-core tellurite nonlinear multimode fibers, avoiding the drilling process or capillary



fabrication for preform build-up. The high nonlinear third-order susceptibility of the glass and the large Raman gain of tellurite glass permit to obtain efficient SC generation in the near-infrared domain with short segments of multimode fibers. In this way, it is possible to preserve the pulse duration and the output peak power large enough for applications such as nonlinear fluorescence imaging. With these fibers, we obtained a SC spanning from 800 to 1700 nm. Such multimode polychromatic beam is used in turn to demonstrate 2PA and 3PA fluorescence imaging with a spatial resolution close to 1.2  $\mu\text{m}$ , when the central wavelength of the incident beam is 1.38  $\mu\text{m}$ . The ease with which these experiments have been carried out demonstrates that nonlinear fluorescence imaging can be simply implemented with acceptable performances when extreme resolution is not required. Due to the spectral domain covered by our SC, it is possible to envisage a M-CARS-type experiment. However, progress in the spectral power density obtained at the end of the fiber and a verification of the low depletion of the pump wave must be obtained before a test.

## 5. Experimental Section

**Glass Synthesis:** Tellurite glasses were prepared from mixed precursors by the melt-quenching method. Samples were prepared under room atmosphere with 99.9% pure  $\text{TeO}_2$  from Fox Chemicals and 99.9% pure  $\text{ZnO}$  and  $\text{La}_2\text{O}_3$  from Alfa Aesar. Oxide precursors were weighed and mixed into a platinum crucible and heated in an electric furnace at 850  $^\circ\text{C}$  for 1 h, before being poured into a brass mold, preheated during 1.5 h at 45  $^\circ\text{C}$  below the glass transition temperature ( $T_g$ -45  $^\circ\text{C}$ ). The sample was then annealed at  $T_g$ -10  $^\circ\text{C}$  to reduce residual mechanical strains.

**Characterizations Methods on Bulk Samples:** Transition temperature was obtained by employing a Q1000 model TA Instrument apparatus to perform differential scanning calorimetry (DSC) on small vitreous bulk samples and thermal expansion coefficient (TEC) was measured for temperatures between 130 and 310  $^\circ\text{C}$  using a Netzsch 402 PC dilatometer.

Refractive index measurements at 543.5, 633, 1064, and 1550 nm were performed with a  $\text{TiO}_2$  prism coupler refractometer homemade setup on one face mirror polished bulk samples.

Raman gains were obtained from spontaneous Raman intensities acquired using an XploRA PLUS (Horiba) spectrometer with two laser sources at 532 and 785 nm focused on the mirror-polished sample surfaces via a 100 $\times$  (N.A. 0.9) objective lens. Spectra of tellurite samples were collected during 10 s and the reference (fused-silica) during 180 s because of its lower Raman intensity. The intensity of samples was then normalized to the peak Raman intensity of fused silica (for a Raman Shift of 440  $\text{cm}^{-1}$ ) to become  $I_{\text{norm}}$ .<sup>[29]</sup> Other correction factors must be applied to correct some optical and thermal effects.<sup>[27]</sup> Reflection losses were corrected with a factor  $F_R$

$$F_R = \frac{(1 + n_{\text{TZL}})^4}{(1 + n_{\text{SiO}_2})^4} \quad (1)$$

With  $n_{\text{TZL}}$  and  $n_{\text{SiO}_2}$  ( $\approx 1.461$  for 532 nm and 1.454 for 785 nm), respectively, refractive index of TZL samples and fused-silica.

Low wavenumber thermal effects are then eliminated by dividing normalized intensity by a Bose–Einstein factor  $F_{\text{BE}}$

$$F_{\text{BE}} = 1 + \left[ \exp\left(\frac{h\nu}{kT}\right) - 1 \right]^{-1} \quad (2)$$

where  $h$  is the Planck's constant ( $h = 6.63 \times 10^{-34}$  J s),  $\nu$  is the frequency of the Raman Shift,  $k$  the Boltzmann constant ( $k = 1.38 \times 10^{-23}$  J  $\text{K}^{-1}$ ), and  $T$ (K) the temperature during the experiment.

Raman gain of the sample  $g_{\text{R(TZL)}}$  is then approximated by the following formula

$$g_{\text{R(TZL)}} = I_{\text{norm}} \times F_R \times \frac{1}{F_{\text{BE}}} \times \left(\frac{n_{\text{SiO}_2}}{n_{\text{TZL}}}\right)^2 \times g_{\text{R(SiO}_2)} \quad (3)$$

With  $g_{\text{R(SiO}_2)} = 1.86 \times 10^{-13}$   $\text{m W}^{-1}$  is the peak Raman gain of the fused-silica for a pump wavelength at 532 nm and a Raman shift of 440  $\text{cm}^{-1}$ <sup>[21]</sup> and  $g_{\text{R(SiO}_2)} = 1.20 \cdot 10^{-13}$   $\text{m W}^{-1}$  is the peak Raman gain of the fused-silica for a pump wavelength at 785 nm.<sup>[22]</sup>

**Fiber Drawing:** Drawing consists of elongation of the glass preform using a 3 m high optical fiber tower. Preform is introduced into an annular furnace under a helium atmosphere and the temperature is heated up by 10  $^\circ\text{C min}^{-1}$  up beyond 400  $^\circ\text{C}$  to reach the glasses softening regime temperature and to initiate drawing.

**Numerical Simulations/Methods:** The simulations have been carried out with a Beam Propagation Method based on the Fourier transform with a spatial (rectangular grid of 90  $\mu\text{m} \times 90 \mu\text{m}$ ) and metallic boundary conditions. The rectangular distribution of the refractive index was modeled by a simplified function of the form  $n(x, y, \omega) = n_0(\omega) + \Delta n \times \exp((-x^8/R_x^8) - (-y^8/R_y^8))$ , with  $R_x = 17.5 \mu\text{m}$ ,  $R_y = 15 \mu\text{m}$ , and  $\Delta n = 1.9 \times 10^{-2}$ .  $n_0(\omega)$  is the frequency dependent refractive index of the core, with the Sellmeier equation taken from ref. [12]. The input pulse duration was of 300 fs and the input beam shape was Gaussian with an FWHM diameter of 18  $\mu\text{m}$ . To lead the formation of irregular speckles, the input beam was tilted by 2.5 $^\circ$  and 1.5 $^\circ$  along the  $x, y$ -axis respectively.

The nonlinear coefficient was  $n_2 = 4 \times 10^{-19}$   $\text{m}^2 \text{W}^{-1}$ . The Raman fraction contribution was modeled by considering a fraction contribution  $f_R = 0.18$  and a Lorentzian profile (see ref. [32] for details) setting the values of time constants  $\tau_1 = 7$  fs and  $\tau_2 = 32$  fs.

## Acknowledgements

This research was funded by the French ANR, project TRAFIC, grant number ANR-18-CE08-0016-03. This work benefited from the facilities of the SMARTLIGHT platform funded by the French ANR (EQUIPEX+ contract "ANR-21-ESRE-0040") and the Région Bourgogne Franche-Comté. It has been supported by the EUR EIPHI Graduate School, grant number ANR-17-EURE-0002 and by the ISITE-BFC grant number ANR-15-IDEX-003 through the 4DMeta project.

## Conflict of Interest

The authors declare no conflict of interest.

## Data Availability Statement

The data that support the findings of this study are available from the corresponding author upon reasonable request.

## Keywords

multimodal imagery, optical fibers, rectangular section, supercontinuum, tellurite

Received: July 26, 2022

Revised: November 21, 2022

Published online: December 9, 2022

[1] C. Kerbage, B. J. Eggleton, *Opt. Photonics News* **2002**, 13, 38.

[2] J. M. Dudley, G. Genty, S. Coen, *Rev. Mod. Phys.* **2006**, 78, 1135.

- [3] J. K. Ranka, R. S. Windeler, A. J. Stentz, *Opt. Lett.* **2000**, *25*, 25.
- [4] C. Poudel, C. F. Kaminski, *J. Opt. Soc. Am. B* **2019**, *36*, A139.
- [5] D. M. Grant, D. S. Elson, D. Schimpf, C. Dunsby, J. Requejo-Isidro, E. Auksorius, I. Munro, M. A. A. Neil, P. M. W. French, E. Nye, G. Stamp, P. Courtney, *Opt. Lett.* **2005**, *30*, 3353.
- [6] N. O. Moussa, T. Mansuryan, C.-H. Hage, M. Fabert, K. Krupa, A. Tonello, M. Ferraro, L. Leggio, M. Zitelli, F. Mangini, A. Niang, G. Millot, M. Papi, S. Wabnitz, V. Couderc, *Sci. Rep.* **2021**, *11*, 18240.
- [7] E. Kakkava, B. Rahmani, N. Borhani, U. Teğin, D. Loterie, G. Konstantinou, C. Moser, D. Psaltis, *Opt. Fiber Technol.* **2019**, *52*, 101985.
- [8] Z. Eslami, L. Salmela, A. Filipkowski, D. Pysz, M. Klimczak, R. Buczynski, J. M. Dudley, G. Genty, *Nat. Commun.* **2022**, *13*, 2126.
- [9] R. El Mallawany, in *Tellurite Glasses Handbook, Physical Properties and Data*, 2nd ed., Taylor & Francis Group, Boca Raton, USA **2012**.
- [10] R. El-Mallawany, M. D. Abdalla, I. A. Ahmed, *Mat. Chem. Phys.* **2008**, *109*, 291.
- [11] P. Froidevaux, A. Lemièrre, B. Kibler, F. Désévéday, P. Mathey, G. Gadret, J.-C. Jules, K. Nagasaka, T. Suzuki, Y. Ohishi, F. Smektala, *Appl. Sci.* **2018**, *8*, 1875.
- [12] A. Maldonado, M. Evrard, E. Serrano, A. Crochetet, F. Désévéday, J. C. Jules, G. Gadret, C. H. Brachais, C. Strutynski, Y. Ledemi, Y. Messaddeq, F. Smektala, *J. Alloy. Compd.* **2021**, *867*, 159042.
- [13] M. Evrard, T. Combes, A. Maldonado, F. Désévéday, G. Gadret, C. Strutynski, J. C. Jules, C. H. Brachais, F. Smektala, *Opt. Mater. Express* **2022**, *12*, 136.
- [14] W. Li, D. Chen, Q. Zhou, L. Hu, *Chin. Opt. Lett.* **2016**, *14*, 011402.
- [15] A. L. Bullington, P. H. Pax, A. K. Sridharan, J. E. Heebner, M. J. Messerly, J. W. Dawson, *Appl. Opt.* **2012**, *51*, 84.
- [16] C. Strutynski, R. A. Meza, L. Teulé-Gay, G. El-Dib, A. Poulon-Quintin, J. Salvétat, L. Vellutini, M. Dussauze, T. Cardinal, S. Danto, *Adv. Funct. Mater.* **2021**, *31*, 2011063.
- [17] A. Plößl, *Mater. Sci. Eng., R* **1999**, *25*, 1.
- [18] R. Jeng, T. Kishi, N. Matsushita, T. Yano, *Int. J. Appl. Sci.* **2019**, *10*, 248.
- [19] I. Savelii, J. C. Jules, G. Gadret, B. Kibler, J. Fatome, M. El-Amraoui, N. Manikandan, X. Zheng, F. Désévéday, J. M. Dudley, J. Troles, L. Brilland, G. Renversez, F. Smektala, *Opt. Mater.* **2011**, *33*, 1661.
- [20] X. Shen, G. Cheng, L. Zhang, W. Wei, *J. Lumin.* **2020**, *227*, 117540.
- [21] R. H. Stolen, C. Lee, *J. Opt. Soc. Am. B* **1984**, *1*, 652.
- [22] Y. Zhang, Y. Xu, C. You, D. Xu, J. Tang, P. Zhang, S. Dai, *Opt. Express* **2017**, *25*, 8886.
- [23] W. K. Bischel, M. J. Dyer, *J. Opt. Soc. Am. B* **1986**, *3*, 677.
- [24] G. P. Agrawal, in *Guided Wave Optical Components and Devices*, Elsevier, San Diego, USA **2006**, pp. 131–153.
- [25] M. F. S. Ferreira, in *Encyclopedia of Modern Optics*, Elsevier, Oxford, UK **2005**, pp. 297–308.
- [26] C. Rivero, R. Stegeman, M. Couzi, D. Talaga, T. Cardinal, K. Richardson, G. Stegeman, *Opt. Express* **2005**, *13*, 4759.
- [27] G. Guery, A. Fargues, T. Cardinal, M. Dussauze, F. Adamietz, V. Rodriguez, J. D. Musgraves, K. Richardson, P. Thomas, *Chem. Phys. Lett.* **2012**, *554*, 123.
- [28] R. Stegeman, C. Rivero, K. Richardson, G. Stegeman, P. Delfyett Jr, Y. Guo, A. Pope, A. Schulte, T. Cardinal, P. Thomas, J.-C. Champarnaud-Mesjard, *Opt. Express* **2005**, *13*, 6.
- [29] M. D. O'Donnell, K. Richardson, R. Stolen, C. Rivero, T. Cardinal, M. Couzi, D. Furniss, A. B. Seddon, *Opt. Mater.* **2008**, *30*, 946.
- [30] M. Ferraro, F. Mangini, M. Zitelli, A. Tonello, A. De Luca, V. Couderc, S. Wabnitz, *Photon. Res.* **2021**, *9*, 2443.
- [31] K. Krupa, A. Tonello, A. Barthélémy, V. Couderc, B. M. Shalaby, A. Bendahmane, G. Millot, S. Wabnitz, *Phys. Rev. Lett.* **2016**, *116*, 183901.
- [32] G. P. Agrawal, *Nonlinear Fiber Optics*, Academic Press, London, UK; San Diego, CA **2019**.